2012

Rate and Apparent Quantum Yield of Photodissolution

Meg Estapa
Skidmore College

Lawrence M. Mayer

Emmanuel Boss

Rate and apparent quantum yield of photodissolution of sedimentary organic matter

Margaret L. Estapa,[a,b,1,*] Lawrence M. Mayer,[a] and Emmanuel Boss [b]

[a] School of Marine Sciences, University of Maine, Darling Marine Center, Walpole, Maine
[b] School of Marine Sciences, University of Maine, Orono, Maine

Abstract

We quantified rates of photochemical dissolution (photodissolution) of organic carbon in coastal Louisiana suspended sediments, conducting experiments under well-defined conditions of irradiance and temperature. Optical properties of the suspended sediments were characterized and used in a radiative transfer model to compute irradiances within turbid suspensions. Photodissolution rate increased with temperature (T), with activation energy of 32 ± 7 kJ mol^{-1}, which implicates indirect (non-photochemical) steps in the net reaction. In most samples, dissolved organic carbon (DOC) concentration increased approximately linearly with time over the first 4 h of irradiation under broadband simulated sunlight, after higher rates in the initial hour of irradiation. Four-hour rates ranged from 2.3 μmol DOC m^{-3} s^{-1} to 3.2 μmol DOC m^{-3} s^{-1}, but showed no relation to sample origin within the study area, organic carbon or reducible iron content, or mass-specific absorption coefficient. First-hour rates were higher—from 3.5 μmol DOC m^{-3} s^{-1} to 7.8 μmol DOC m^{-3} s^{-1}—and correlated well with sediment reducible iron (itself often associated with organic matter). The spectral apparent quantum yield (AQY) for photodissolution was computed by fitting DOC photoproduction rates under different spectral irradiance distributions to corresponding rates of light absorption by particles. The photodissolution AQY magnitude is similar to most published dissolved-phase AQY spectra for dissolved inorganic carbon photoproduction, which suggests that in turbid coastal waters where particles dominate light absorption, DOC photoproduction from particles exceeds photooxidation of DOC.

Recent laboratory studies have demonstrated that under solar irradiance, significant amounts of particulate organic carbon (POC) in suspended marine and aquatic particles can be photochemically released as dissolved organic carbon (DOC). Under simulated sunlight, Mayer et al. (2006), Kieber et al. (2006), and Riggsbee et al. (2008) induced photochemical POC dissolution (photodissolution) in resuspended sediments in coastal and freshwater environments. Photodissolution of POC from Louisiana sediments leads to O$_2$ consumption, dissolved inorganic carbon (DIC) production, peroxide production (Estapa and Mayer 2010), and loss of lignin, bromine, and Δ^{14}C-modern carbon from particles (Mayer et al. 2009*a*). Particle-hosted photochemical reactions are not limited to mineral-rich coastal sediments; irradiation of algal cellular detritus results in similar photodissolution extents (Mayer et al. 2009*b*). Irradiation of particles from both coastal and oliogotrophic regimes results in efficient production of carbon monoxide (Xie and Zafiriou 2009).

Such photochemical transformations could affect fluxes of carbon through marine systems in a variety of ways. For instance, burial of POC in shallow sediments is an important removal term in coastal carbon budgets that could be reduced by sediment resuspension and subsequent POC photodissolution. In the overlying coastal water column, photochemical production of DOC from suspended particulate matter (SPM) and episodically resuspended sediments may provide DOC to microbes and to cross-shelf transport (Mayer et al. 2011). Offshore, sunlight contributes to the photochemical alteration of detrital particles, as evidenced by photochemical degradation products in lipids from sinking and suspended particulates (Rontani et al. 2011). Photochemical reactions may also affect the cycling of iron–organic complexes (Waite 2005).

Solar irradiance varies substantially as a function of wavelength, time, location, and depth within the water column, and particulate absorption coefficients in the environment depend on highly variable suspended particle concentrations. Quantitative estimates of particle-hosted, photochemical reaction rates thus require knowledge of their spectral efficiency, or apparent quantum yield (AQY). To our knowledge, only one marine particulate photochemistry study to date reports particulate absorption coefficients (Xie and Zafiriou 2009), and Mayer et al. (2006) only qualitatively accounted for absorbed irradiance within experimental suspensions. Here, we use an experimental approach to estimate the spectral AQY of one particulate photoreaction, POC photodissolution, for a collection of coastal SPM samples from Louisiana. We also quantify the positive temperature-dependence of the photodissolution rate indicated by Mayer et al. (2006). Finally, we examine the dependence of photodissolution rate on the particles' light absorption coefficients, reducible iron, and organic carbon contents.

Methods

To account for irradiance absorbed by particles, we require a radiative transfer model that is valid for turbid water and one that describes scalar irradiance attenuation in terms of measureable radiometric quantities and particle

* Corresponding author: mestapa@whoi.edu

[1] Present address: Marine Chemistry and Geochemistry Department, Woods Hole Oceanographic Institution, Woods Hole, Massachusetts

optical properties. Below, we derive this model from prior photochemical work in non-scattering water. Next, we describe our experimental design, and finally our sample analytical techniques.

Definitions—The AQY is the photochemical reaction rate normalized to the light absorption rate of the reacting substance (Eq. 1). The adjective 'apparent' is necessary in the case of organic matter in the environment because neither the chemical concentrations of the actual reacting molecules, nor their relative contributions to the measured total absorption coefficient, are known. We define the AQY as

$$AQY(\lambda) = \frac{\dfrac{d[DOC]}{dt}}{Q(\lambda)} \tag{1}$$

where $d[DOC]/dt$ refers to the production rate of DOC (μmol DOC m^{-3} s^{-1}), and $Q(\lambda)$ (μE m^{-3} s^{-1}) refers to the rate of light absorption by the photoreacting substance as a function of wavelength (λ). $Q(\lambda)$ is the depth-integrated product of scalar irradiance and the absorption coefficient of the photoreacting substance, normalized to the reaction volume:

$$Q(\lambda) = \frac{SA}{V} \int_{-\infty}^{0} E_o(\lambda, z) \times a_x(\lambda) dz \tag{2}$$

Above, SA (m^2) and V (m^3) are, respectively, the area of the upper surface and the volume of the reaction volume, $E_o(\lambda, z)$ is scalar irradiance (μE m^{-2} s^{-1}) as a function of wavelength and depth z (m), and $a_x(\lambda)$ is the absorption coefficient of the reacting substance (for simplicity, we assume that all inherent optical properties are constant with respect to depth). If light scattering is negligible (i.e., in the absence of particles), Eq. 2 can be integrated with respect to depth and $Q(\lambda)$ computed according to Eq. 3 (following Hu et al. 2002; wavelength notation dropped for brevity):

$$Q = E_d(0^-) \times (1 - e^{-a_t H}) \times \frac{SA}{V} \times \frac{a_x}{a_t} \tag{3}$$

where a_t (m^{-1}) is the total absorption coefficient (including water and dissolved substances), $E_d(0^-)$ (μE m^{-2} s^{-1}) is the area-normalized rate of downward light flux to a depth just below the surface, and H (m) is the depth of the reaction volume. The dimensionless term $(1 - e^{-a_t H})$ is the fraction of light not absorbed above depth H.

In the case of water with a non-negligible particle concentration, light is both scattered and absorbed, and the computation of Q must also account for scattering losses of light from the experimental volume. Figure 1 shows a schematic of the experimental volume and the irradiance quantities discussed in our derivation of Q for scattering water, below. In a horizontally infinite system, or one bounded by specularly reflecting (mirror-like) walls, these depth-integrated scattering losses equal the sum of light lost from the upper air–water interface and absorbed by the bottom. Gershun's law, derived for a plane-parallel medium (Eq. 4; Gershun 1939), states that the depth rate

of change of net (i.e., vector) irradiance, defined as the downward minus the upward irradiance ($E_{net} \equiv E_d - E_u$), equals the scalar irradiance times the absorption coefficient within the water:

$$\frac{dE_{net}(z)}{dz} = -a_t(z) \times E_o(z) \tag{4}$$

Integrating Eq. 4 over depth from just below the surface (0^-) to the bottom of the finite volume H, light absorbed within the volume (Eq. 2) is equivalent to the difference between $E_{net}(0^-)$ and $E_{net}(H)$:

$$E_{net}(0^-) - E_{net}(H) = \int_{H}^{0^-} E_o(z) \times a_t \, dz \tag{5}$$

Conservation of energy requires that net irradiance remain constant above and below the air–water interface of the experimental volume ($E_{net}(0^-) = E_{net}(0^+)$; Fig. 1), so after defining above-water reflectance as the ratio of upward to downward planar irradiance ($R(0^+) = E_u(0^+) / E_d(0^+)$), we can express Q as follows:

$$\begin{aligned} Q &= \frac{SA}{V} \int E_o(z) \times a_x \, dz \\ &= \frac{a_x}{a_t} \times \frac{SA}{V} \times [E_d(0^+) \times (1 - R(0^+)) - E_{net}(H)] \end{aligned} \tag{6}$$

In Eq. 6, the irradiance lost to scattering back through the air–water interface is parameterized through the irradiance reflectance R, while irradiance lost from the bottom of the experimental volume is $E_{net}(H)$. In this general formulation (Eq. 6), the surface H could represent, for instance, a physical interface (the bottom of a cell) or an arbitrary depth within a larger water column. To determine the AQY for a photochemical reaction in scattering media, we therefore must know not only $E_d(0^+, \lambda)$, $a_x(\lambda)$, and $a_t(\lambda)$; as in Eq. 3 for non-scattering media; Hu et al. 2002), but also the irradiance reflectance $R(0^+, \lambda)$ and the net irradiance at the bottom of the experimental volume, $E_{net}(\lambda, H)$.

Experimental design rationale—To determine $Q(\lambda)$ for suspensions of absorbing and scattering particles examined in this study, we express $E_{net}(\lambda, H)$ in terms of the depth-averaged net irradiance attenuation coefficient $<K_{net}(\lambda)>$ (Eq. 7; Fig. 1), which scales approximately directly with the concentration of absorbing particles and will permit a more general discussion below. By rewriting $E_{net}(\lambda, H)$ in terms of $<K_{net}(\lambda)>$ (Eq. 7), we assume $Q(\lambda)$ is independent of the optical properties of the experimental volume's boundaries (explicit in Eq. 6). This assumption is justified at large optical depths (i.e., deep enough that nearly all incident light is attenuated within the sample volume, as in our experiments), where the optical properties of the bottom surface at H have only a small effect on $Q(\lambda)$,

$$\begin{aligned} Q(\lambda) = \frac{a_x(\lambda)}{a_t(\lambda)} &\times \frac{SA}{V} (E_d(\lambda, 0^+) \times (1 - R(\lambda, 0^+))) \\ &\times (1 - e^{-<K_{net}(\lambda)>H}) \end{aligned} \tag{7}$$
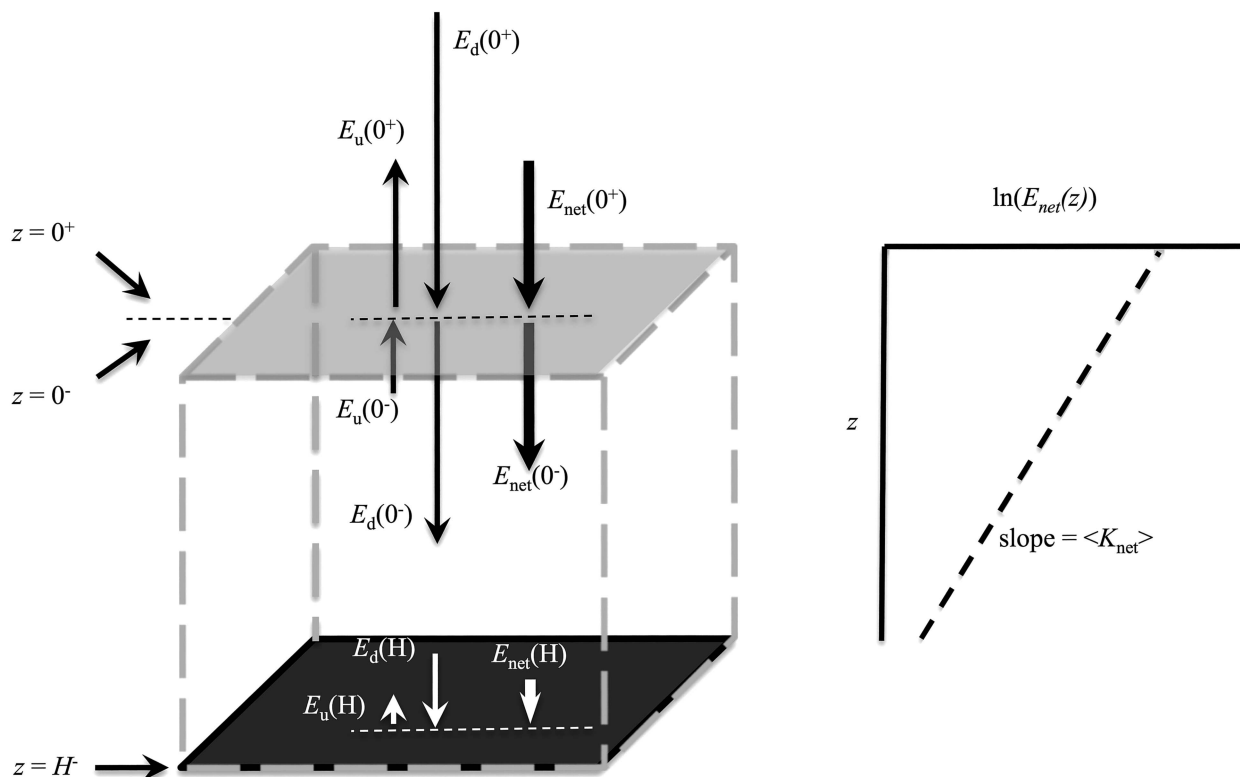
Fig. 1. Schematic showing irradiance quantities defined in text. (A) Dashed-line cube shows hypothetical sample volume within horizontally infinite system. Top face is air–water interface and bottom face is the bottom boundary of the sample volume. Vertical arrows show upward, downward, and net irradiances just above and below air–water interface and above the bottom boundary. Wavelength notation is omitted and arrows are vertical for clarity, although in reality irradiances are functions of wavelength and are integrated over all upward and downward directions. Relative lengths of arrows are proportional to magnitudes of hypothetical irradiances such that $E_{net}(0^+) = E_{net}(0^-)$. (B) Plot at right shows definition of mean net irradiance attenuation coefficient $<K_{net}>$.

Photochemical reactions under constant irradiance can be described using either apparent zero- or first-order kinetics with respect to the reactant (Zepp 1978), depending on whether the reactant concentration changes appreciably during irradiation ('apparent zero-order kinetics' here is equivalent to the initial rate approximation for an apparent first-order reaction). A general rate law (Gordon and Ford 1972), in terms of DOC production from POC, is

$$\frac{d[DOC]}{dt} = k[POC]^n \qquad (8)$$

where n is the reaction order with respect to POC and k is the rate constant. For an apparent first-order reaction, k is defined as

$$k \equiv [POC] \times \int_{\lambda_{min}}^{\lambda_{max}} Q^*(\lambda) \times AQY(\lambda) \, d\lambda$$

$$= \int_{\lambda_{min}}^{\lambda_{max}} Q(\lambda) \times AQY(\lambda) \, d\lambda \qquad (9)$$

where k has units of s^{-1} and $Q^*(\lambda)$ is the POC-specific light absorption rate. Our experiments were designed with high initial POC concentrations, and DOC measurements were made early in the reaction before major POC loss. Therefore, Q defined as in Eq. 7 and computed for the initial suspension (i.e., $Q^* \times [POC]_{initial}$) can be substituted in the rate expression and the reaction described with apparent zero-order kinetics (i.e., with an initial rate approximation), with k bearing units of μmol DOC m^{-3} s^{-1}. Apparent zero-order rate constants, equivalent under our approximation to first-order rate constant times [POC]$_{initial}$ concentration, were determined from the slope of the regression of DOC concentration against time.

Longer term photodissolution experiments (Kieber et al. 2006; Mayer et al. 2006; Estapa and Mayer 2010) have thus far been insufficient to determine the apparent reaction order with respect to POC. In these studies, however, the observed photodissolution rate, measured both as DOC production and POC loss, decreased over exposures longer than 10 h at light intensities similar to this study. This nonlinearity suggests that a true reaction order is at least first-order, consistent with depletion of photolabile POC or another reactant. We justify the initial rate approximation used in this study by considering the dynamics of sediment resuspension often encountered in turbid aquatic environments. High SPM concentrations near the surface may only persist for periods of hours (Grabemann and Krause 1989; Wright et al. 1990; Kineke et al. 2006). While they persist, the wind- or current-driven mixed layer likely extends

Table 1.   Sample summary. SPM = suspended particulate matter; wt = weight; Fe_{dith} = combined content of reducible iron oxides and organic-bound iron; a_p^* = mass-specific absorption.

Sample description	Organic carbon content ($\pm$ 0.2 mg g^{-1})	Fe_{dith} ($\pm$ 0.02 wt % Fe)	$a_p^*(300)$ ($\pm$ 0.01 m^2 g^{-1})
1. Marine SPM, Freshwater Bayou, Apr 2003	20.0	nd*	0.24
2. Marine SPM, Freshwater Bayou, Mar 2008	17.4	1.45	0.22
3. Marine sediment, Atchafalaya River delta, Apr 2008	18.3	1.83	0.21
4. River SPM, Atchafalaya River at Morgan City, Apr 2003	17.5	2.93	0.33
5. River SPM, Mississippi River at Venice, Mar 2004	22.3	1.87	0.23
6. River SPM, Mississippi River at St. Francisville, Dec 2004	28.1	1.96	0.19

* nd = insufficient sample quantity for iron oxide determination.

deeper than the depth of light penetration (order 10^0–10^1 cm), providing a continuous resupply of 'fresh' POC. We utilize optical property data and a simple dynamic model to explore the limits of this initial rate approximation (*see* Discussion, below).

Experimental—Photodissolution rate measurements were conducted using suspended particles and sediments collected from coastal Louisiana and the Mississippi and Atchafalaya rivers. Sediment grabs (box corer or Ekman grab) were used to collect unconsolidated surficial sediments (top 0–1 cm), while SPM samples were isolated from large surface-water volumes via overnight settling or centrifugation. Particles were freeze-dried and stored dry and frozen until optical and photochemical analyses, which should not affect photodissolution extent (Mayer et al. 2006). We selected samples for analysis from a larger set to represent a wide range of particle mass-specific absorption coefficients, organic carbon contents, and reducible iron contents (Table 1). Mass-specific absorption coefficients were measured in suspension in an integrating sphere accessory attached to a spectrophotometer, while dithionite-citrate extraction (Loeppert and Inskeep 1996) was used to determine the combined content of reducible iron oxides and organic-bound iron (Fe_{dith}; *see* Estapa et al. 2012).

To measure rates of photodissolution, samples were sieved to < 63 μm, weighed into replicate, precombusted glass beakers, and covered with precombusted quartz disks. Reflective foil and matte black tape lined the beakers' outer sides and bottoms, respectively. Carbon-clean artificial seawater (containing Na$^+$, Mg^{2+}, K$^+$, Ca^{2+}, Cl$^-$, and SO$_4^{2-}$ in seawater proportions to give salinity ~ 35) was added to create 3-cm-deep particle suspensions with known mass concentrations (~ 500 mg L^{-1}). Suspensions were magnetically stirred from the bottom with carbon-clean, glass-coated stir bars.

Irradiations were conducted in a solar simulator (Atlas Suntest CPS) equipped with a filtered xenon lamp replicating the wavelength distribution of solar irradiance. A thermostatted, recirculating water-bath controlled the temperature (during most experiments) to $\pm$ 1°C (exceptions discussed below). We used 4-h experiments for rate determination under full-spectrum irradiance in order to maintain initial conditions. In this case, the concentration of DOC at time t ([DOC]$_t$) was much less than the initial concentration of POC ([POC]$_0$), which allowed rate

determination following Eq. 8. Samples of DOC were collected at 0 h, 0.5 h, 1 h, 2 h, and 4 h after the start of irradiation. Suspensions were magnetically stirred for 30 min prior to being placed in the solar simulator, so that initial, non-photochemical, desorption would be assessed in the t = 0 h sample. We measured the DOC concentration by removing sets of duplicate beakers from the solar simulator, filtering each suspension through a precombusted glass-fiber filter, and analyzing the filtrates in triplicate with a Shimadzu TOC-V$_{CPH}$ analyzer. POC concentrations at 0 h and 4 h were determined on the glass-fiber filters after vapor-phase acidification and combustion in a Perkin Elmer 2400 elemental analyzer. We computed the photodissolution rate (μmol DOC m^{-3} s^{-1}) for each experiment as the slope of the best linear fit to the mean DOC concentration vs. time data. Uncertainty in the DOC production rate was taken as the uncertainty in this slope.

We assessed the temperature sensitivity of the photodissolution rate by varying the water-bath temperature in a series of replicate 4-h irradiations of a single sample (Atchafalaya River delta sediment, No. 3 in Table 1). Temperatures within identical, tap-water–filled beakers in the solar simulator reached steady-state ($\pm$ 1°C) prior to substitution by, and irradiation of, the sample beakers (usually after 30 min with the lamp on and bath recirculating). Sample beakers removed from the simulator during each time series were replaced with these tap-water–filled beakers to maintain the thermal mass inside the sample chamber. We computed Arrhenius parameters for the temperature dependence of the reaction by iteratively fitting the 4-h rate and temperature data to Eq. 10:

$$\ln(k) = 1000 \times \frac{E_a}{R_g T} - \ln(A) \qquad (10)$$

where E_a represents the reaction activation energy (kJ mol DOC^{-1}), R_g the gas constant, T the reaction temperature (° Kelvin), and A the pre-exponential factor (μmol DOC m^{-3} s^{-1}). A Monte Carlo procedure was used to propagate analytical uncertainty in temperatures and rate constants into the Arrhenius parameters.

In this study, we measured $E_d(0^+,\lambda)$ and the coefficients of mass-specific absorption ($a_p^*(\lambda)$) and scattering ($b_p^*(\lambda)$) of particle samples directly, and used the latter two parameters to derive $a_x(\lambda)$, $a_t(\lambda)$, and total scattering coefficients ($b_t(\lambda)$) for experimental suspensions containing

Table 2. Ecolight® input parameters to simulate laboratory conditions. CDOM = colored dissolved organic matter.

Parameter	Value
Inherent optical property (IOP) model	Case 2 (routine 'abcase2.f')
IOP model components and concentrations	Seawater ($n=1.34$), mineral particles (500 mg L^{-1}), no colored dissolved organic matter (CDOM) or chlorophyll (concentrations=0)
Mass-specific absorption	Empirical sample measurements ($a_p^*(300)$: Table 1; $a_p^*(\lambda)$: Estapa et al. 2012)
Mass-specific beam attenuation	Mean field measurements (Eq. 11)
Chlorophyll and CDOM fluorescence and Raman scattering	None
Wavelength range	300–800 nm, 5-nm increments
Depth range	0–0.03 m, 0.0004-m increments
Bottom depth	0.03 m
Bottom reflectance	0 at all wavelengths (i.e., black bottom)
Wind speed	0 m s^{-1}
Sky model	Semi-empirical, 100% overcast conditions
Sky radiance angular distribution model	'hcnrad' routine
Solar zenith	0° (directly overhead)
Ozone	Mean annual
Earth–sun distance	Mean annual
Total incident irradiance	Solar simulator output spectrum

only water and known particle mass concentrations. We computed $a_x(\lambda)$ as the product of $a_p^*(\lambda)$ and the particle mass concentration, $a_t(\lambda)$ as the sum of $a_x(\lambda)$ and $a_w(\lambda$; known absorption of water), and $b_t(\lambda)$ as the product of $b_p^*(\lambda)$ and the particle mass concentration, plus a small scattering contribution by water. We then entered $E_d(0^+,\lambda)$, $a_t(\lambda)$, and $b_t(\lambda)$ into a radiative transfer model (described below) whose outputs included $R(0^+,\lambda)$ and $\langle K_{net}(\lambda)\rangle$. These last two parameters were then used to compute $Q(\lambda)$ according to Eq. 7.

The solar simulator delivered a constant output irradiance of 765 W m^{-2} (300–800 nm), approximately equivalent to subtropical noontime sunlight, during all experiments. A built-in radiometer calibrated to a National Institute of Standards and Technology–traceable source monitored and controlled the lamp power throughout each experiment. Prior to AQY-determination experiments, we measured the intensity, wavelength, and spatial distribution of the solar simulator's output with nitrate and nitrite actinometers (Jankowski et al. 1999) and with a spectroradiometer (Satlantic HyperOCR irradiance sensor). Spectroradiometer measurements (350–800 nm) were made by collecting time-averaged measurements of $E_d(0^+)$ inside the simulator sample chamber at varying distances from the four walls. We prepared actinometer solutions as described by Jankowski et al. (1999), filled beakers identical to those used in sample irradiations to a depth of 1 cm, and exposed the beakers to simulated sunlight at 765 W m^{-2} for 1 h. Salicylic acid production rates, determined via batch fluorescence measurements, were used to calculate band-integrated incident irradiances (Jankowski et al. 1999) in the nitrate (301–328 nm) and nitrite (324–385 nm) absorption bands. The air–water interfaces of sample suspensions and actinometer solutions, and the sensor face of the radiometer, were all placed at the same level below the xenon lamp in the solar simulator. Spatially averaged radiometric and actinometric irradiance measurements agreed with the nominal irradiance spectrum of the simulator. Irradiances near the

sides of the sample chamber were about 6% below the mean, while those measured near the center of the sample chamber were about 6% above the mean.

We used a radiative transfer model (Ecolight®, Sequoia Scientific) to determine depth-averaged $K_{net}(\lambda)$ and the irradiance reflectance, $R(\lambda)$ for experimental suspensions. The spectral absorption and beam attenuation coefficients of suspensions containing 500 mg L^{-1} suspended sediments and artificial seawater were used as inputs to the model. We used the model's default values for seawater absorption and scattering (Pope and Fry 1997), and assumed a seawater index of refraction of 1.34. Mass-specific absorption spectra of suspended sediment as a function of wavelength were determined using an integrating sphere accessory (Estapa et al. 2012). We determined the mass-specific, beam attenuation spectrum of suspended sediments by regressing field measurements of spectral beam attenuation against simultaneously determined SPM concentrations (*see* below). The angular scattering dependence (volume scattering function) of suspended particles was approximated with a Fournier–Forand phase function with a spectrally invariant particulate backscatter fraction (b_b/b) of 0.02—a typical value for suspended, mostly inorganic particles from this region (Snyder et al. 2008). In Ecolight®, an overcast sky model approximated the diffusing effect of the reflective inner walls of the solar simulator. Additional Ecolight parameters are in Table 2.

Field inherent optical property (IOP) data were collected in turbid areas of coastal Louisiana in the vicinity of sediment and SPM sampling locations (Table 1), and they were used to determine mass-specific beam attenuation and to validate mass-specific absorption spectra of freeze-dried samples. In March of 2008, near-surface optical properties were measured continuously through the flowing seawater system of the R/V *Pelican* during a cruise to the turbid Freshwater Bayou region of coastal Louisiana. Continuously operating instrumentation included a multispectral, absorption and beam attenuation meter (ac9; WETLabs)
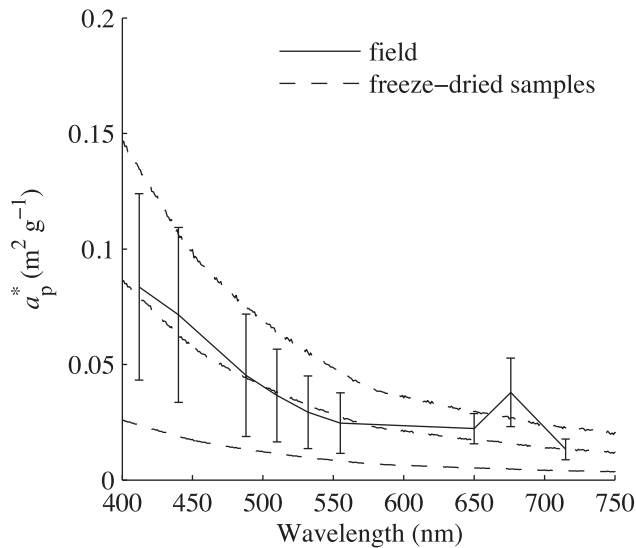
Fig. 2. Comparison of mass-specific absorption spectra measured in the field with an ac9 and on freeze-dried samples in the lab. Field spectrum (solid line) is the median of measurements made when SPM concentrations were between 7 mg L^{-1} and 25 mg L^{-1}, as described in the text. Dashed lines show mean and 95% confidence interval of 25 freeze-dried samples from the study region (*see* Estapa et al. 2012 for details). To account for scattering-correction uncertainties in the ac9 data, the two spectra are forced into agreement at 715 nm by adding a constant y-offset to the field data. Peaks in the field spectrum at 440 nm and 676 nm are due to phytoplankton pigments not evident in the freeze-dried samples, which were collected at higher turbidities.

and a three-angle backscatter meter (EcoVSF; WETLabs), while SPM and colored dissolved organic matter (CDOM) were sampled by filtration from periodic discrete samples. Multispectral beam attenuation and absorption data were corrected for temperature- and salinity-dependent attenuation by water and time binned into 1-min intervals. Absorption data were additionally corrected for scattering losses within the ac9 light path according to the third method of Zaneveld et al. (1994), and CDOM absorption was subtracted. SPM concentrations were determined gravimetrically on triplicate, pretared, 0.1-μm pore size, 47-mm-diameter polycarbonate filters (Nucleopore). The slope of the regression line between the raw backscattering signal and simultaneously measured SPM concentration was used to obtain a continuous SPM proxy from the EcoVSF.

Multispectral, mass-specific particulate beam attenuation ($c_p^*(\lambda)$) and absorption ($a_p^*(\lambda)$) were determined from the slopes of the linear regressions between the SPM backscatter proxy and corrected beam attenuation and absorption spectra, over SPM concentrations between 7 mg L^{-1} and 25 mg L^{-1}. The lower limit excluded low suspended-sediment waters, while the upper limit excluded measurements potentially affected by multiple scattering within the ac9 light path (Leymarie et al. 2010). A power-law function (Eq. 11; Boss et al. 2001) fit the derived $c_p^*(\lambda)$ vs. wavelength data well, and was used to extrapolate c_p^* through the 300–800-nm range needed for the radiative transfer model:

$$c_p^*(\lambda) = c_p^*(531)\left(\frac{\lambda}{531}\right)^{-0.89}; \ c_p^*(531) = 1 \ \text{m}^2\text{g}^{-1} \quad (11)$$

The scattering correction applied to the ac9 absorption data is known to underestimate true absorption in highly scattering waters and in the presence of significant non-water absorption at 715 nm (Tzortziou et al. 2006; Leymarie et al. 2010), while absorption measured with our integrating sphere setup is subject to minimal scattering losses (Babin and Stramski 2002). To enable comparison, a spectrally flat offset was added back into the field data to force the two data sets into agreement at a_p^* (715). After this correction, the mean $a_p^*(\lambda)$ spectrum from the field data was similar in magnitude and variability to the mean mass-specific absorption of 25 freeze-dried suspended and sedimented samples collected from the same region and measured in the laboratory with the integrating sphere (Fig. 2; Estapa et al. 2012). Spectral absorption features characteristic of phytoplankton pigments and degradation products are present in the field data but not in the freeze-dried samples, likely because the latter were collected at higher turbidities.

We computed net irradiance as a function of wavelength and depth ($E_{net}(\lambda,z)$) as the difference between $E_d(\lambda,z)$ and $E_u(\lambda,z)$ output from the radiative transfer model. The net irradiance attenuation coefficient $K_{net}(\lambda)$ was computed as the mean of the derivative with respect to depth of $\ln(E_{net}(\lambda,z))$. We calculated the irradiance reflectance above the air–water interface ($R(\lambda,0^+)$) as the output ratio of upward to downward irradiance just above the air–water interface.

The above-water reflectance $R(0^+,\lambda)$ and the mass-specific, net particulate attenuation coefficient ($K_{p,net}^*(\lambda,$ SPM)) were recomputed in Ecolight® for varying concentrations of suspended particles (10^1–10^3 mg L^{-1}) in order to assess sensitivity of our results (all from 500 mg L^{-1} suspensions) to varying SPM concentration. $K_{p,net}^*(\lambda,\text{SPM})$ was computed as

$$K_{p,net}^*(\lambda,\text{SPM}) = (K_{net}(\lambda,\text{SPM}) - a_w(\lambda))/\text{SPM} \quad (12)$$

($K_{net}(\lambda,\text{SPM})$ − $a_w(\lambda)$) scaled roughly with the SPM concentration (not shown) but $K_{p,net}^*(\lambda,\text{SPM})$ decreased slightly as SPM increased (Fig. 3a), reflecting path-length amplification due to increased scattering. $K_{p,net}^*(\lambda,\text{SPM})$ was well-approximated by ($a_p^*(\lambda) + b_{bp}^*(\lambda)$) / 0.7 (Gordon 1989; Fig. 3a). Above SPM concentrations of about 250 mg L^{-1}, $R(0^+)$ varied little at ultraviolet (UV) wavelengths (Fig. 3b).

The depth-integrated irradiance absorbed within the suspension by sediment particles ($Q(\lambda)$) was finally computed according to Eq. 7. To determine the spectral AQY for POC photodissolution, DOC photoproduction from a single sample (Atchafalaya River delta sediment, No. 3 in Table 1) was measured under a series of long-pass wavelength filters (300 nm, 400 nm, 500 nm, 600 nm, and 700 nm) following the method of Johannessen and Miller (2001). Polyester lighting filters (Lee Filters) shielded the entire solar-simulator sample chamber. Filter transmission
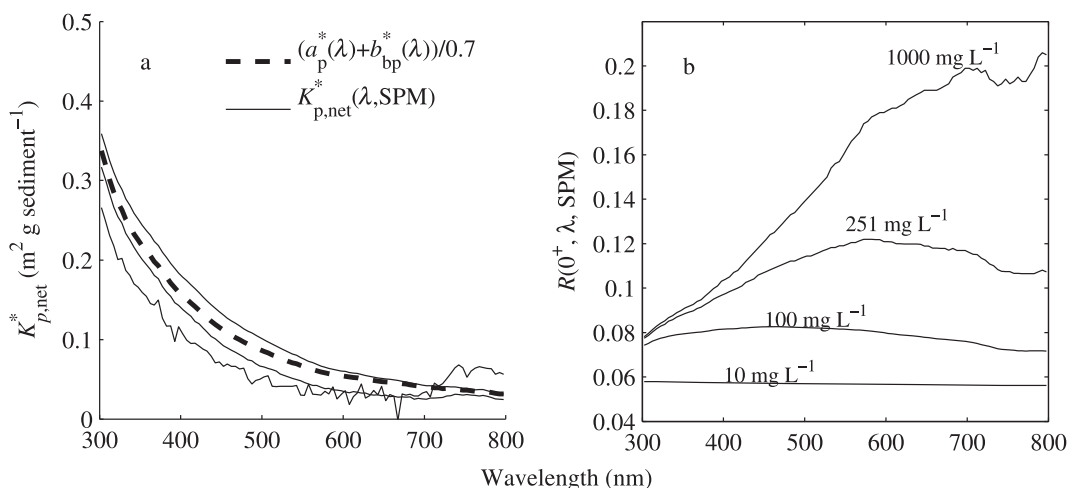
Fig. 3. $R(0^+,\lambda)$ and $K^*_{p,\text{net}}(\lambda)$ as a function of SPM concentration. (a) shows $K^*_{p,\text{net}}(\lambda)$ for SPM log-spaced at 10^1, 10^2, and 10^3 mg L^{-1} in thin solid lines, with arrow indicating direction of increasing concentration. Thick dashed line shows $K^*_{p,\text{net}}(\lambda)$ approximated as $(a^*_p + b^*_{bp}) / 0.7$ (Gordon 1989). (b) shows $R(0^+,\lambda)$ as a function of SPM for selected log-spaced concentrations. Above about 250 mg L^{-1}, $R(0^+)$ is relatively invariant at ultraviolet wavelengths.

was constant during the irradiation treatments. In order to produce measurable DOC concentrations under reduced photon energies, we increased irradiation times from 4 h to 5 h, 8 h, 12 h, and 46 h in respective treatments under 400 nm, 500 nm, 600 nm, and 700 nm long-pass filters, but maintained the same relative sampling frequency and linear increase of DOC vs. time described above for full spectrum irradiations. We computed the AQY using a modification of the statistical curve fit method described by Johannessen and Miller (2001). Spectral irradiance absorbed in each treatment was computed from Eq. 7, above, where $E_d(\lambda,0^+)$ was the measured irradiance in the solar simulator, the relative particulate absorption spectrum $a_x(\lambda)/a_t(\lambda)$ was computed from the known mass concentration of suspended sediment and the IOPs of sediments and water, and $R(\lambda)$ and $K_{\text{net}}(\lambda)$ were output from Ecolight®. Many AQY spectra for photoreactions of marine CDOM are well-described by an exponential function (Eq. 13, Johannessen and Miller 2001):

$$\text{AQY}(\lambda) = \text{AQY}(290) \times e^{(-S(\lambda-290))} \quad (13)$$

We found that Eq. 13 similarly describes the wavelength-dependence of photodissolution (*see* Results). We estimated the amplitude (AQY(290)) and slope (S) parameters by iteratively minimizing Eq. 14 (using Matlab® function 'fminsearch'):

$$y = \sum \left[\frac{1}{Q(\lambda)} \frac{d\text{DOC}}{dt} - A\tilde{Q}Y(290)\exp(-\tilde{S} \times (\lambda - 290)) \right]^2 \quad (14)$$

where $Q(\lambda)$ was computed according to Eq. 7. Finally, a Monte Carlo procedure was used to propagate the uncertainty in the DOC production rate into the parameters AQY(290) and S.

To compensate for increasing photodissolution rates as a function of temperature (Mayer et al. 2006), rates and AQYs reported below have been recalculated, according

to an Arrhenius rate model (Eq. 15), to a reference temperature of 25°C (298 K).

$$\text{Rate}_{298K} = \text{Rate}_T \times e^{-\frac{E_a}{R_g}(1/298 - 1/T)} \quad (15)$$

where T is the temperature (in ° Kelvin) of the suspension, and Rate_{298K} and Rate_T refer, respectively, to the rates at 298K and at the original temperature. The activation energy (E_a) for photodissolution, determined from rate measurements between 17° and 29°C, was 32 ± 7 kJ mol^{-1} (Fig. 4). The fit of the data to the Arrhenius model was best above 19°C (Fig. 4). Temperature normalization changed the rates reported below by < 14% for all samples.

Results

Photodissolution rates during the first hour of irradiation (Table 3; Fig. 5) correlated positively with sample Fe$_{\text{dith}}$ content (Table 1; Fig. 5). After the first hour, DOC photoproduction increased approximately linearly with time (Fig. 5). The relationship between first-hour photodissolution rate and sample Fe$_{\text{dith}}$ ($n = 4$, $R^2 = 0.97$, $p = 0.013$) did not persist for the full 4-h irradiation treatment (Table 3). Normalization of the 1-h photodissolution rates to modeled scalar irradiance absorbed by particles at 350 nm ($Q(350)$, μmol DOC nm μE^{-1}) did not remove the dependence on sample Fe$_{\text{dith}}$ (Fig. 6a). No strong relationships existed between $Q(350)$-normalized rates over either time period, and sample organic carbon content or mass-specific absorption (Fig. 7b,c).

Irradiance reflectance ($R(\lambda)$) ranged among samples from 7–8.5% at 300 nm to 16–18% at 700 nm (Fig. 7a). The net irradiance attenuation coefficient ($K_{\text{net}}(\lambda)$) ranged from 165–222 m^{-1} at 300 nm to 14–19 m^{-1} at 700 nm (Fig. 7b). Attenuation depths (Fig. 7c) were similar to those measured by Mayer et al. (2006) via actinometry in 450-mg
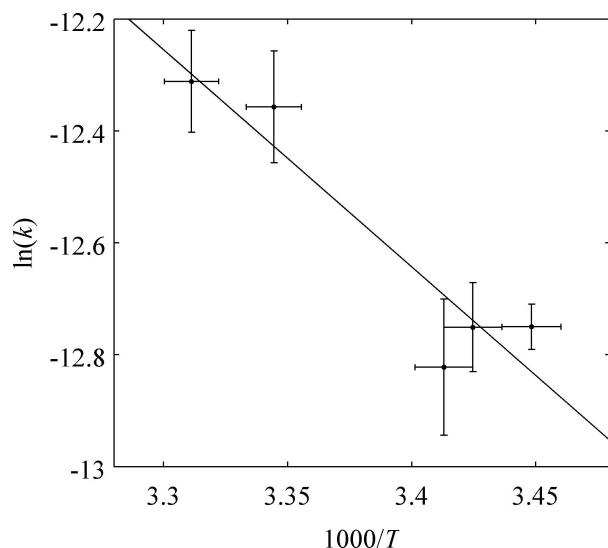
Fig. 4. Arrhenius plot of 4-h rates measured in tests of photodissolution temperature dependence. Arrhenius parameters: $-E_a / R_g$ (slope) = -3.9 ± 0.9K; $\ln(A)$ (intercept) = 2 ± 30 μmol DOC m^{-3} s^{-1}. Error bars are derived from analytical uncertainty in temperature ($\pm 1^\circ$C) and rate.

L^{-1} sediment suspensions, although differences in the solar simulator and container walls prohibit quantitative comparison. The fraction of surface irradiance reaching the bottom of the suspensions (Fig. 7d) shows that > 90% of < 400-nm light passing the air–water interface was absorbed within the suspension, and > 75% at wavelengths < 500 nm, thus confirming 'optically thick' conditions at photochemically important UV and blue wavelengths.

In suspensions exposed to long-pass–filtered sunlight, photodissolution rates decreased as the wavelength of incident irradiance increased (Table 4), but visible wavelengths drove a substantial portion of the reaction. POC photodissolved at a rate of 2.4 ± 0.2 μmol DOC m^{-3} s^{-1} under the 300-nm long-pass filter, and 1.2 ± 0.1 μmol DOC m^{-3} s^{-1} under the 400-nm filter. Smaller, but still significant, reaction rates were observed under 500 nm, 600 nm, and 700 nm long-pass filters (Table 4).

Space limitations did not permit us to measure temperature in wavelength-filtered experiments to the same precision achieved in the broadband irradiations. We tested the sensitivity of AQY(290) and S to uncertainty in the temperature measurement by scaling long-pass–filtered photodissolution rates (measured at $19 \pm 2^\circ$C) to

temperatures ranging from 10° to 35°C (using results of temperature-sensitivity experiments; *see* Eq. 15 and Fig. 4). The subsequently computed AQY spectral slope, S, did not vary as a function of temperature, but the pre-exponential term AQY(290) did. We therefore recomputed AQY(290) separately for all broadband experiments (for which accurate temperatures were available), while assuming a constant value of S determined from long-pass cut-off experiments (Eq. 16).

$$\mathrm{AQY}(290) = \frac{\dfrac{d[\mathrm{DOC}]}{dt}}{e^{-S(\lambda - 290)} \times Q(\lambda)} \qquad (16)$$

The AQY spectral slope determined from long-pass–filtered experiments was 0.017 ± 0.003 nm^{-1}, while AQY(290) values computed from broadband irradiations of samples listed in Table 3 ranged from 0.0007 μmol DOC μE^{-1} to 0.0009 μmol DOC μE^{-1} (Table 3). The resulting AQY spectra for all samples are shown in Fig. 8. As a test, the derived AQY spectrum for the Atchafalaya delta sediment (Sample 3 in Table 1) was used to predict DOC production rates in the individual long-pass filter experiments listed in Table 4 (which were conducted with the same sediment sample). The fit between measured and modeled DOC production rates in these experiments had a root mean-squared error of 0.094 μmol DOC m^{-3} s^{-1}, which was less than the analytical uncertainty in most of the rate determination experiments (Table 3). The alternate, 'quasi-exponential' AQY functional form of Bélanger et al. (2006) was tested, but the minimization function did not converge (regardless of the initial solution guess used for the iterative fitting routine), suggesting that the quasi-exponential model does not describe these data well.

Discussion

From a mechanistic standpoint, the photodissolution AQY reported here cannot be easily compared to published dissolved-phase marine AQY spectra, because the relative contents of absorbing-but-photoresistant compounds in POC are probably different from those in CDOM (Zafiriou 2002). From a modeling standpoint, however, such comparisons are useful, because AQY spectra allow us to estimate in situ photoreaction rates from a waterbody's radiometric and optical properties (Bélanger et al. 2008). This rationale led us to compute the photodissolution AQY

Table 3. Photodissolution rates (95% CI) adjusted to $T = 25^\circ$C (μmol DOC m^{-3} s^{-1}). SPM = suspended particulate matter; AQY = apparent quantum yield.

| Sample description	1-h rate	4-h rate	Measurement temperature (°C)	4-h AQY(290) ($\times 10^{-4}$ μmol μE^{-1})
1. Marine SPM, Freshwater Bayou, Apr 2003	3.79(0.06)	2.3(0.5)	25	7(2)
2. Marine SPM, Freshwater Bayou, Mar 2008	3.5(0.5)	2.7(0.1)	22	8(1)
3. Marine sediment, Atchafalaya River delta, Apr 2008	5.0(0.8)	3.0(0.3)	17–31	9(2)
4. River SPM, Atchafalaya River at Morgan City, Apr 2003	7.8(0.4)	2.6(0.7)	25	7(2)
5. River SPM, Mississippi River at Venice, Mar 2005	4.18(0.05)	3.2(0.2)	26	9(2)
6. River SPM, Mississippi River at St. Francisville, Dec 2004	nd*	2.5(0.4)	25	7(2)

* nd = lost 0.5-h sample, so 1-h rate not determined.
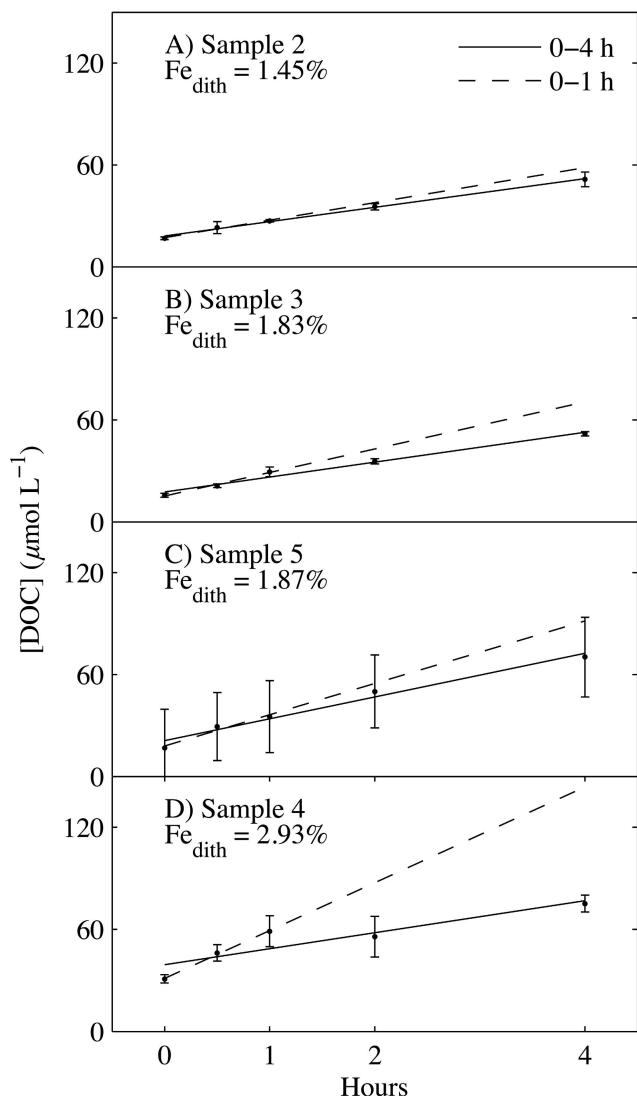
Fig. 5. Photoproduced DOC concentration, as a function of time under simulated sunlight, for the four samples in which both Fe$_{dith}$ content and 0–1-h rates were determined (Samples 2–5; Tables 2 and 3). Solid lines show best fit to [DOC] vs. time data over 4 h and dashed lines show best fit over the first hour only. Error bars show analytical uncertainty in DOC concentration. Root mean-squared (RMS) error for 4-h linear fit ranged from 1 μmol L^{-1} DOC (Sample 2) to 6 μmol L^{-1} DOC (Sample 4). Samples were mixed for 30 min prior to irradiation; hence, the non-zero $t = 0$ h DOC concentrations.

relative to the total, rather than organic carbon- or Fe$_{dith}$-specific, particulate absorption coefficients.

DIC is the most-abundant, identifiable photoproduct of CDOM. Figure 9 shows the photodissolution AQY computed in this study alongside AQY spectra for DIC photoproduction from CDOM, pooled for temperate 'inshore' waters (Johannessen and Miller 2001) and Arctic shelf waters (Bélanger et al. 2006). The AQY for DOC production via photodissolution is comparable to or greater than the CDOM AQYs. This similarity suggests that POC photodissolution may occur in nearshore waters even in the presence of significant, competing CDOM
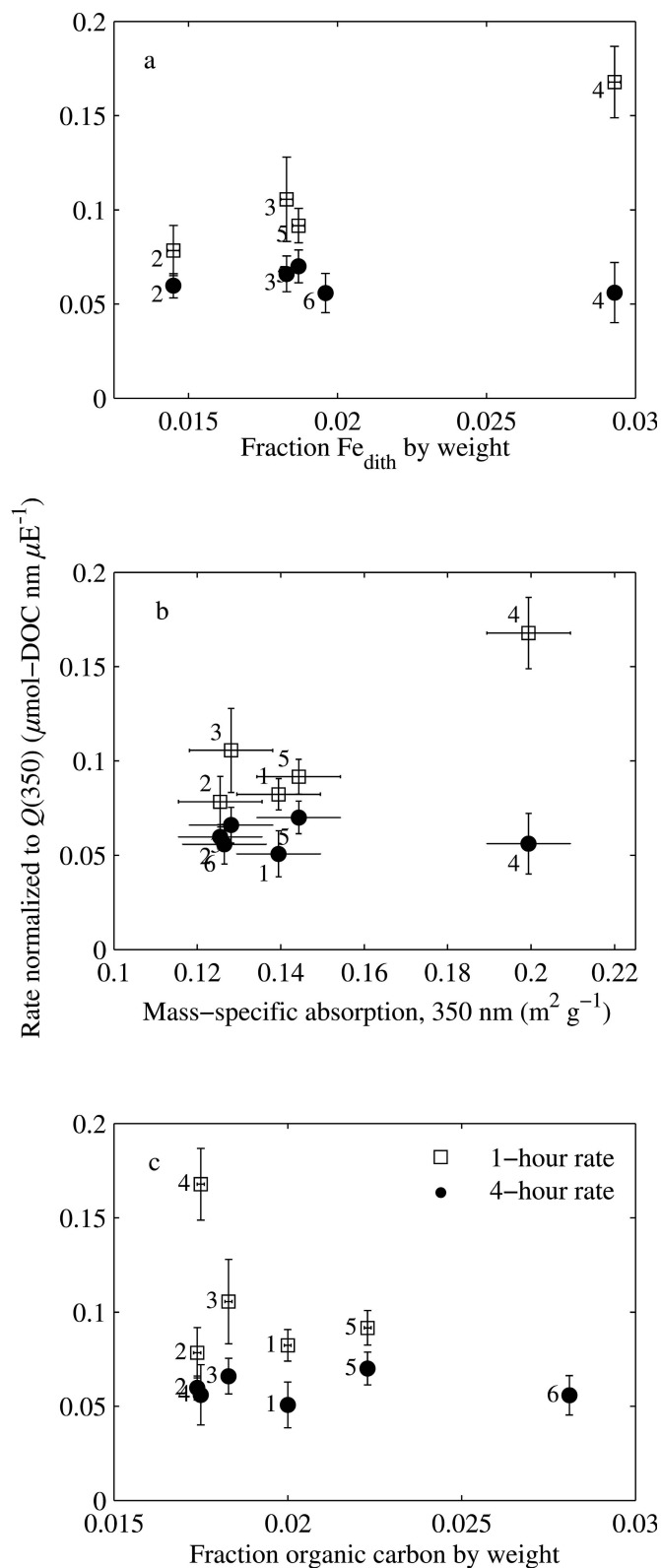

Fig. 6. Photodissolution rates normalized to absorbed irradiance at 350 nm (Rate/Q(350)), computed over 1-h (open squares) and 4-h (filled circles). (a) Rate/Q(350) as a function of suspended sediment Fe$_{dith}$. (b) Rate/Q(350) vs. particulate mass-specific absorption at 350 nm. (c) Rate/Q(350) as a function of suspended sediment organic carbon fraction. Error bars represent analytical uncertainties and labels correspond to sample numbers in Tables 1 and 2.
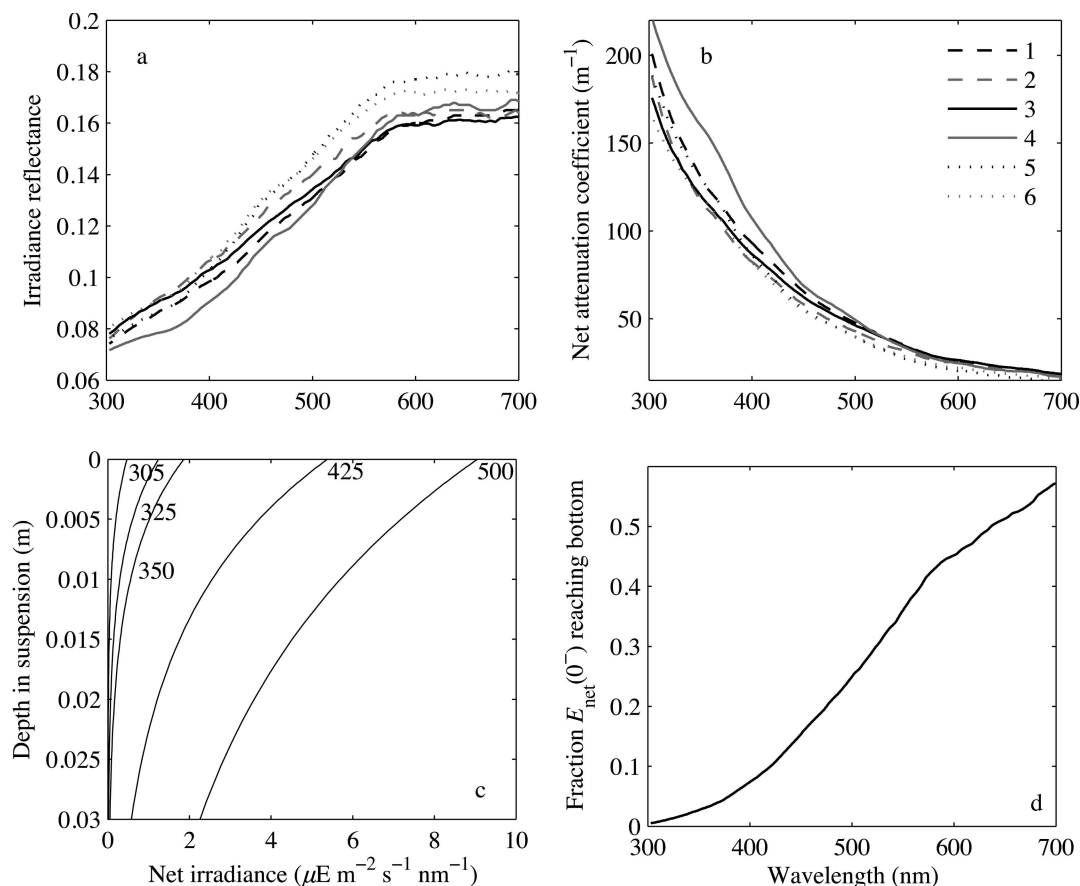
Fig. 7. Radiative transfer model outputs. (a) Irradiance reflectance just above the air–water interface ($R(0^+)$), with line shading and pattern representing samples as organized in Tables 1 and 2. (b) Net irradiance attenuation coefficient ($K_{net}(\lambda)$) within 500 mg L^{-1} suspension, with patterns as in (a). (c) Net irradiance within suspension of Atchafalaya River delta sediment (Sample 3) as a function of depth and selected wavelengths ($E_{net}(z,\lambda)$). (d) Fraction of net irradiance (just below surface) reaching the bottom (at 3 cm) of suspension of Atchafalaya River delta sediment.

absorption. By multiplying the photodissolution AQY by the mean DIC : DOC photoproduction ratio (0.45) measured in ~ 20-h irradiations of suspended Louisiana coastal sediments (Estapa and Mayer 2010), we have computed a rough AQY estimate for DIC photoproduction from particles. The magnitude of this estimated AQY is less certain because it is based on a DIC : DOC photoproduction ratio determined during much longer irradiation periods (Estapa and Mayer 2010). Even so, this estimate of particulate DIC photoproduction is comparable to DIC photoproduction from CDOM in temperate, inshore waters and Arctic shelf waters (Fig. 9). This calculation implies that suspended sediment-dominated nearshore waters may contribute to DIC photoproduction as much as do CDOM-dominated waters further offshore.

The significant, positive temperature dependence of the POC photodissolution rate (Fig. 4) suggests that although the net reaction may be initiated photochemically, it also involves subsequent, diffusion-limited steps. While direct photochemical reactions often have very low activation energies, thermally driven (non-photochemical) reactions have much higher values. We computed a moderate E_a value for photodissolution, 32 $\pm$ 7 kJ mol^{-1}, which is somewhat higher than rarely determined activation energies

of dissolved-phase, marine organic photochemical reactions: 12.2 kJ mol^{-1} for CO photoproduction (Zhang et al. 2006), 13 kJ mol^{-1} for domoic acid photolysis (Bouillon et al. 2006), and 23 kJ mol^{-1} for near-surface DMS photolysis (Toole et al. 2003). The phase change inherent to photodissolution (i.e., desorption or dissolution of POC) may account for the increased activation energy of this reaction. The Arrhenius model does not fit the data well at the low end of the temperature range investigated (Fig. 4), which may be due to imprecise temperature control or changing reaction kinetics as a function of temperature. Our temperature-dependence data agree with Mayer et al. (2006), who observed that a decrease in temperature from ~ 35–40°C to 23°C reduced the 24-h extent of reaction by one-third. The temperature range investigated here (17–30°C) includes much of the annual range of water temperatures observed in the study region of coastal Louisiana.

We have assumed that the true photodissolution reaction order is at least first-order with respect to SPM, because light absorption by particles scales with SPM concentration and with POC concentration early in the reaction (Eq. 9). We did not explicitly test for a higher order dependence of photodissolution rate on SPM concentration, but prior

Table 4. Photodissolution rates in long-pass–filtered experiments ($T = 19 \pm 2°C$). DOC = dissolved organic carbon.

Cut-off wavelength (nm)	Length of experiment (h)	Rate (μmol-DOC m^{-3} s^{-1})
300	4	2.4(0.2)
400	5	1.2(0.1)
500	8	0.26(0.08)
600	12	0.14(0.08)
700	46	0.08(0.02)

results provide guidance in this respect. Estapa and Mayer (2010) showed that 24-h photodissolution extents were identical in continuously stirred beakers and sealed test tubes shaken by hand every 6–8 h. This equivalence suggests a minor effect of particle–particle collisions (which depend on differential particle velocity) on the photodissolution rate.

Unlike CDOM, which photobleaches (absorption decreases) as the light dose increases (Andrews et al. 2000), lengthy UV exposures negligibly photobleach suspended, primarily inorganic particles, although dominance of absorption by iron (Estapa et al. 2012) may mask bleaching of organic matter. Therefore, consumption of a photoreactive substrate for this photodissolution reaction might not be accompanied by measurable photobleaching of the overall particulate substrate, in contrast to photobleaching of dissolved materials, which partially explains the dose-dependence of their photochemical rates (Andrews et al. 2000).

The correlation between Fe_{dith} and initial photodissolution rates (Fig. 5) suggests ligand-to-metal charge transfer reactions in iron–organic complexes, which would photo-oxidize (and possibly dissolve) the organic ligands while photoreducing Fe^{3+} to Fe^{2+} (Moffett and Zafiriou 1993). Irradiation of suspended sediments similar to those in this study caused the total iron content of small (0.7–8.0-μm diameter) particles to increase, which is consistent with rapid reoxidation and precipitation of photoreduced iron (Estapa and Mayer 2010), a process also observed by Kopáček et al. (2005) during photodegradation of dissolved organic–metal complexes in lakes. Variable, yet non-negligible, amounts of organic carbon are adsorbed or complexed to dithionite-reducible iron in marine sediments both globally (Lalonde et al. 2012) and in the Mississippi river and delta system (Mayer et al. unpubl.), consistent with release of DOC during photoreductive dissolution of the iron. However, Mayer et al. (2006) found that removal of dithionite-reducible iron prior to irradiation of suspended sediments did not affect the longer term (tens of hours) extent of organic carbon photodissolution. From these findings, we infer that iron photoredox processes may influence the high photodissolution rates observed in the first hour of irradiation, but that they become less important over longer timescales (Table 3; Fig. 6). The uniformity of $Q(350)$-normalized 4-h rates reported here (Fig. 6; mean $\pm$ 1 SD = 0.060 $\pm$ 0.007 μmol DOC nm μE^{-1}) is consistent with other reports showing remarkably similar long-term ($\sim$ 20 h) photodissolution extents (21–24%) among seasonally and compositionally varying samples (Mayer et al. 2006).
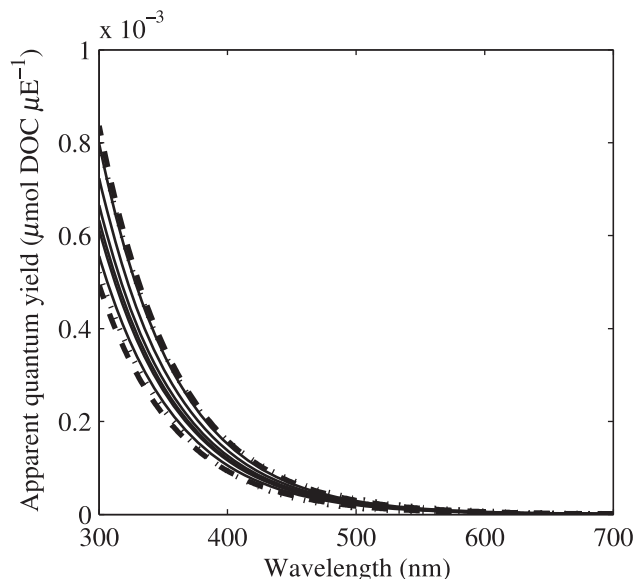

Fig. 8. Apparent quantum-yield spectra for photodissolution. Thin solid lines show spectra for individual samples listed in Table 2. Heavy dashed lines denote twice the standard deviation of the measured sample set. Heavy dotted lines show single-sample analytical uncertainty propagated from uncertainty in AQY spectral slope parameter ($S = 0.0166 \pm 0.003$ nm^{-1}) and measured photodissolution rates (*see* Table 2).

Particle suspensions used to determine photodissolution rates were uniformly mixed through the 3-cm-deep photic zone (Fig. 7c). To correctly extrapolate these reported rates to environmental conditions, we must consider local variations in incident sunlight, mixing depth and intensity, and suspended particle concentration. Under turbid conditions (> 10 mg L^{-1} suspended sediment), we can compute attenuation coefficients (Fig. 7b) over varying suspended sediment concentrations to estimate the depth of UV- and blue-wavelength light penetration ($z_{5\%}$, here defined as 3 optical depths, or the 5% light level). A particle settling from the surface under low-energy conditions, with velocity ω_s, will spend an amount of time in the photic zone equivalent to $t_{settling} = z_{5\%}/\omega_s$. Under high-energy conditions, a particle mixed repeatedly from surface to bottom of the water column or mixed layer (z_{mixing}) will spend equal amounts of time at all depths $< z_{mixing}$, and thus will be exposed to light for the time-integral of the ratio $z_{5\%} : z_{mixing}$. In Fig. 10 we illustrate these low- and high-energy cases for suspended sediment concentrations ranging from 10^1 mg L^{-1} to 10^3 mg L^{-1}, for $z_{mixing} = 1$–10 m, and integrated over solar irradiance time periods representative of the summer and winter solstices in coastal Louisiana. These calculations show that when SPM concentration exceeds $\sim 10^2$ mg L^{-1}, a given particle is likely exposed to 350-nm light for < 1 h d^{-1} regardless of water-column depth (for $z_{mixing} > 1$ m) or day length. Below this approximate SPM concentration, $z_{5\%}$ deepens, and daily exposure times increasingly depend upon z_{mixing} and the day length. Therefore, the AQYs computed here over 4-h time periods likely underestimate rates of photodissolution occurring in the field, especially at low
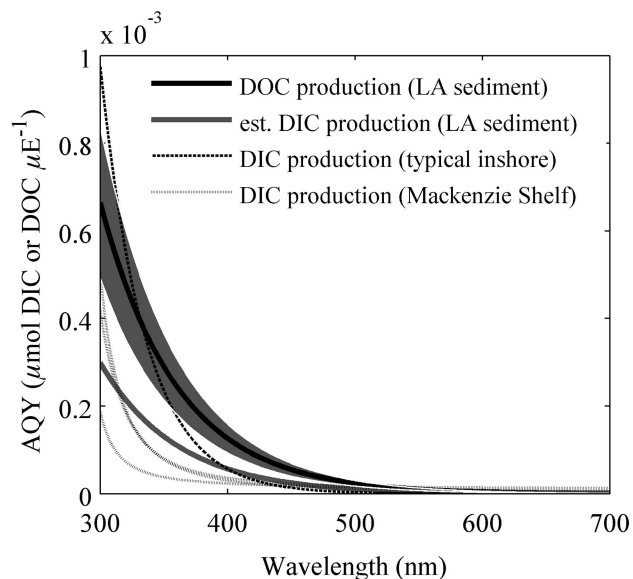
Fig. 9.   Mean ± twice standard deviation of photodissolution AQY spectra measured in this study (thick black line and shaded gray area) along with literature examples of dissolved-phase DIC production AQY spectra. Long-dashed line shows the mean AQY for DIC photoproduction from 'inshore' CDOM at several pooled sites (Johannessen and Miller 2001). Dotted lines show AQY estimates for DIC photoproduction from CDOM at Mackenzie shelf stations in the Arctic (Bélanger et al. 2006). Thick, gray line is an estimate of the particulate DIC photoproduction AQY, based on a 0.45 ratio of DIC : DOC production in Louisiana (LA) coastal suspended sediments (Estapa and Mayer 2010).

irradiances (e.g., low solar zenith angles and overcast conditions) and when suspended sediments have high Fe_{dith} content.

The Fe_{dith}-dependence of the initial rates measured here suggests that in situ photodissolution may be enhanced at sites characterized by episodic resuspension. Aller (2004) postulated that redox-state oscillation of iron and manganese in muddy sediments, driven by periodic resuspension events, could enhance benthic organic carbon remineralization during intervening calm periods by renewing oxidants in the sediments. To the extent that sedimentary Fe^{2+} is present in sediments and pore waters, and is reoxidized during resuspension, oscillating redox conditions might periodically increase reducible iron concentrations at the surface, and thus enhance photodissolution in the upper water column.

Using an approach combining laboratory experiments and radiative transfer modeling to characterize light levels within turbid sediment suspensions, we have presented the first photodissolution rate measurements under well-characterized irradiance conditions. These irradiance- and absorption-normalized measurements are necessary for quantitative prediction of the in situ extents of biogeochemically relevant, particle-hosted photoreactions, especially in shallow embayments, estuaries, and marshes where light absorption rates of suspended particles and dissolved materials are both significant. Because the AQY for photodissolution is similar in magnitude to DIC photoproduction from CDOM, relative light absorption rates of particulate and dissolved organic matter in these
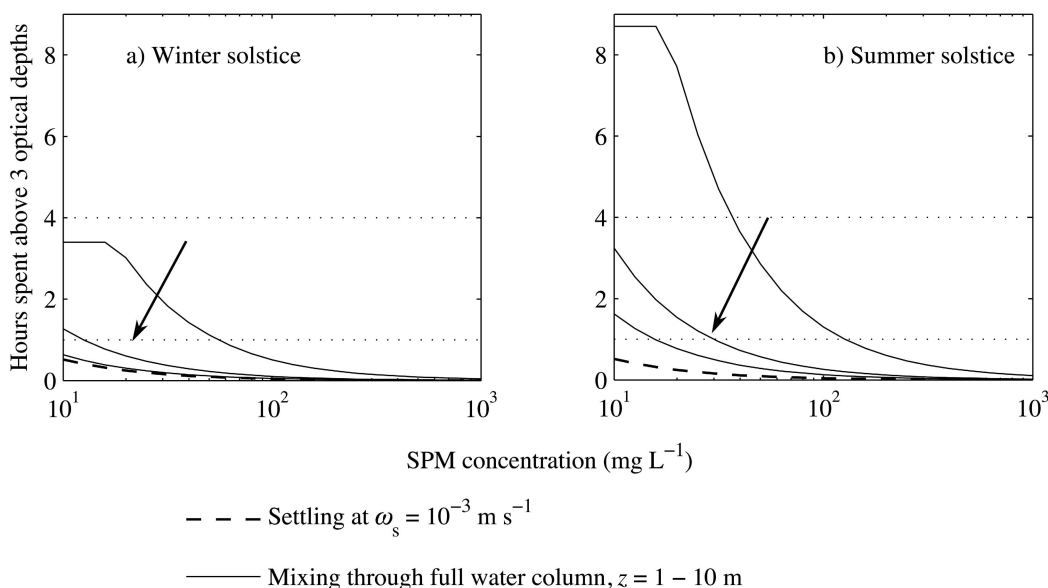

Fig. 10.   Schematic showing approximate length of time a hypothetical particle would be exposed to sunlight of 350 nm under different mixing and optical conditions. Exposure time is assumed to equal the time spent more shallow than three optical depths (i.e., 5% light level) in a mixed layer or water column 1 m, 5 m, or 10 m thick (thin solid lines; arrow shows direction of increasing depth) with sediment concentration ranging from 10 mg L^{-1} to 1000 mg L^{-1}. (a) assumes 3.4 h d^{-1} of high sun-angle ($<$ 57°) sunlight penetration into the water, equivalent to winter solstice in coastal Louisiana, and (b) shows 8.7 h d^{-1}, equivalent to the summer solstice. Arrows show direction of increasing depth. Thick lines on both panels show exposure time based only on the canonical settling speed ($\omega_s = 10^{-3}$ m s^{-1}; Hill et al. [1998]) of an aggregate starting at the surface. Thin dashed lines denote 1-h and 4-h time periods over which reaction rates were measured in the present study. Optical depths were computed from $K_{net}(\lambda)$ values for different SPM concentrations but no other absorbing constituents except pure seawater.

environments should control the relative importance of photoproduction of DOC from particles and photooxidative DOC loss from the dissolved phase. A rigorous whole-water, photochemical carbon budget will thus require spatiotemporally resolved estimates of light absorption by each component.

References

ALLER, R. 2004. Conceptual models of early diagenetic processes: The muddy seafloor as an unsteady, batch reactor. J. Mar. Res. **62:** 815–835, doi:10.1357/0022240042880837

ANDREWS, S. S., O. C. ZAFIRIOU, AND S. CARON. 2000. Photochemical oxygen consumption in marine waters: A major sink for colored dissolved organic matter? Limnol. Oceanogr. **45:** 267–277, doi:10.4319/lo.2000.45.2.0267

BABIN, M., AND D. STRAMSKI. 2002. Light absorption by aquatic particles in the near-infrared spectral region. Limnol. Oceanogr. **47:** 911–915, doi:10.4319/lo.2002.47.3.0911

BÉLANGER, S., M. BABIN, AND P. LAROUCHE. 2008. An empirical ocean color algorithm for estimating the contribution of chromophoric dissolved organic matter to total light absorption in optically complex waters. J. Geophys. Res. **113:** C04027, doi:10.1029/2007JC004436

———, H. XIE, N. KROTKOV, P. LAROUCHE, W. F. VINCENT, AND M. BABIN. 2006. Photomineralization of terrigenous dissolved organic matter in Arctic coastal waters from 1979 to 2003: Interannual variability and implications of climate change. Glob. Biogeochem. Cycles **20:** GB4005, doi:10.1029/2006GB002708

BOSS, E., M. S. TWARDOWSKI, AND S. HERRING. 2001. Shape of the particulate beam attenuation spectrum and its inversion to obtain the shape of the particulate size distribution. Appl. Opt. **40:** 4885–4893, doi:10.1364/AO.40.004885

BOUILLON, R.-C., T. L. KNIERIM, R. J. KIEBER, S. A. SKRABAL, AND J. L. C. WRIGHT. 2006. Photodegradation of the algal toxin domoic acid in natural water matrices. Limnol. Oceanogr. **51:** 321–330, doi:10.4319/lo.2006.51.1.0321

ESTAPA, M. L., AND L. M. MAYER. 2010. Photooxidation of particulate organic matter, carbon/oxygen stoichiometry, and related photoreactions. Mar. Chem. **122,** 138–147, doi:10.1016/j.marchem.2010.06.003

———, E. BOSS, L. M. MAYER, AND C. S. ROESLER. 2012. Role of iron and organic carbon in mass-specific light absorption by particulate matter from Louisiana coastal waters. Limnol. Oceanogr. **57:** 97–112, doi:10.4319/lo.2012.57.1.0097

GERSHUN, A. A. 1939. The light field. J. Math Phys. **18:** 51–151.

GORDON, A. J., AND R. A. FORD. 1972. Chemist's companion—a handbook of practical data, techniques, and references. John Wiley & Sons.

GORDON, H. R. 1989. Can the Lambert–Beer law be applied to the diffuse attenuation coefficient of ocean water? Limnol. Oceanogr. **34:** 1389–1409, doi:10.4319/lo.1989.34.8.1389

GRABEMANN, L., AND G. KRAUSE. 1989. Transport processes of suspended matter derived from time series in a tidal estuary. J. Geophys. Res. **94:** 14373–14379, doi:10.1029/JC094iC10p14373

HILL, P. S., J. P. SYVITSKI, E. A. COWAN, AND R. D. POWELL. 1998. In situ observations of floc settling velocities in Glacier Bay, Alaska. Mar. Geol. **145:** 85–94, doi:10.1016/S0025-3227(97)00109-6

HU, C., F. E. MULLER-KARGER, AND R. G. ZEPP. 2002. Absorbance, absorption coefficient, and apparent quantum yield: A comment on common ambiguity in the use of these optical concepts. Limnol. Oceanogr. **47:** 1261–1267.

JANKOWSKI, J. J., D. J. KIEBER, AND K. MOPPER. 1999. Nitrate and nitrite ultraviolet actinometers. Photochem. Photobiol. **70:** 319–328, doi:10.1111/j.1751-1097.1999.tb08143.x

JOHANNESSEN, S. C., AND W. L. MILLER. 2001. Quantum yield for the photochemical production of dissolved inorganic carbon in seawater. Mar. Chem. **76:** 271–283, doi:10.1016/S0304-4203(01)00067-6

KIEBER, R. J., R. F. WHITEHEAD, AND S. A. SKRABAL. 2006. Photochemical production of dissolved organic carbon from resuspended sediments. Limnol. Oceanogr. **51:** 2187–2195, doi:10.4319/lo.2006.51.5.2187

KINEKE, G. C., E. E. HIGGINS, K. HART, AND D. VELASCO. 2006. Fine-sediment transport associated with cold-front passages on the shallow shelf, Gulf of Mexico. Cont. Shelf Res. **26:** 2073–2091, doi:10.1016/j.csr.2006.07.023

KOPÁČEK, J., Š. KLEMENTOVÁ, AND S. A. NORTON. 2005. Photochemical production of ionic and particulate aluminum and iron in lakes. Environ. Sci. Technol. **39:** 3656–3662, doi:10.1021/es048101a

LALONDE, K., A. MUCCI, A. OUELLET, AND Y. GELINAS. 2012. Preservation of organic matter in sediments promoted by iron. Nature **483:** 198–200, doi:10.1038/nature10855

LEYMARIE, E., D. DOXARAN, AND M. BABIN. 2010. Uncertainties associated to measurements of inherent optical properties in natural waters. Appl. Opt. **49:** 5415–5436, doi:10.1364/AO.49.005415

LOEPPERT, R. H., AND W. P. INSKEEP. 1996. Iron, p. 639–664. *In* D. L. Sparks [ed.], Methods of soil analysis. Part 3: Chemical methods. Soil Science Society of America.

MAYER, L. M., L. L. SCHICK, T. S. BIANCHI, AND L. A. WYSOCKI. 2009a. Photochemical changes in chemical markers of sedimentary organic matter source and age. Mar. Chem. **113:** 123–128, doi:10.1016/j.marchem.2009.01.006

———, ———, K. R. HARDY, AND M. L. ESTAPA. 2009b. Photodissolution and other photochemical changes upon irradiation of algal detritus. Limnol. Oceanogr. **54:** 1688–1698, doi:10.4319/lo.2009.54.5.1688

———, ———, K. SKORKO, AND E. BOSS. 2006. Photodissolution of particulate organic matter from sediments. Limnol. Oceanogr. **51:** 1064–1071, doi:10.4319/lo.2006.51.2.1064

———, K. H. THORNTON, AND L. L. SCHICK. 2011. Bioavailability of organic matter photodissolved from coastal sediments. Aquat. Microb. Ecol. **64:** 275–284, doi:10.3354/ame01530

MOFFETT, J. W., AND O. C. ZAFIRIOU. 1993. The photochemical decomposition of hydrogen peroxide in surface waters of the eastern Caribbean and Orinoco River. J. Geophys. Res. **98:** 2307–2313, doi:10.1029/92JC02768

POPE, R. M., AND E. S. FRY. 1997. Absorption spectrum (380–700 nm) of pure water. II. Integrating cavity measurements. Appl. Opt. **36:** 8710–8723, doi:10.1364/AO.36.008710

RIGGSBEE, J., C. ORR, D. LEECH, M. DOYLE, AND R. WETZEL. 2008. Suspended sediments in river ecosystems: Photochemical sources of dissolved organic carbon, dissolved organic nitrogen, and adsorptive removal of dissolved iron. J. Geophys. Res. **113:** G03019, doi:10.1029/2007JG000654

RONTANI, J.-F., N. ZABETIA, AND S. G. WAKEHAM. 2011. Degradation of particulate organic matter in the equatorial Pacific Ocean: Biotic or abiotic? Limnol. Oceanogr. **56:** 333–349, doi:10.4319/lo.2011.56.1.0333

SNYDER, W. A., AND OTHERS. 2008. Optical scattering and backscattering by organic and inorganic particulates in US coastal waters. Appl. Opt. **47:** 666–677, doi:10.1364/AO.47.000666

TOOLE, D. A., D. J. KIEBER, R. P. KIENE, D. A. SIEGEL, AND N. B. NELSON. 2003. Photolysis and the dimethylsulfide (DMS) summer paradox in the Sargasso Sea. Limnol. Oceanogr. **48:** 1088–1100, doi:10.4319/lo.2003.48.3.1088

TZORTZIOU, M., J. R. HERMAN, C. L. GALLEGOS, P. J. NEALE, A. SUBRAMANIAM, L. W. HARDING, JR., AND Z. AHMAD. 2006. Bio-optics of the Chesapeake Bay from measurements and radiative transfer closure. Estuar. Coast. Shelf Sci. **68:** 348–362, doi:10.1016/j.ecss.2006.02.016

WAITE, T. 2005. Role of iron in light-induced environmental processes, p. 255–298. *In* P. Boule, D. Bahnemann, and P. Robertson [eds.], Environmental photochemistry part II. Springer Berlin/Heidelberg.

WRIGHT, L. D., W. J. WISEMAN, JR., Z.-S. YANG, B. D. BORNHOLD, G. H. KELLER, D. B. PRIOR, AND J. N. SUHAYDA. 1990. Processes of marine dispersal and deposition of suspended silts off the modern mouth of the Huanghe (Yellow River). Cont. Shelf Res. **10:** 1–40, doi:10.1016/0278-4343(90)90033-I

XIE, H., AND O. C. ZAFIRIOU. 2009. Evidence for significant photochemical production of carbon monoxide by particles in coastal and oligotrophic marine waters. Geophys. Res. Lett. **36:** L23606, doi:10.1029/2009GL041158

ZAFIRIOU, O. C. 2002. Sunburnt organic matter: Biogeochemistry of light-altered substrates. Limnol. Oceanogr. Bull. **11:** 69–71.

ZANEVELD, J. R. V., J. C. KITCHEN, AND C. M. MOORE. 1994. The scattering error correction of reflecting-tube absorption meters. Proc. SPIE Ocean Opt. XII **2258:** 44–55, doi:10.1117/12.190095

ZEPP, R. G. 1978. Quantum yields for reaction of pollutants in dilute aqueous solution. Water Resour. Res. **12:** 327–329.

ZHANG, Y., H. XIE, AND G. CHEN. 2006. Factors affecting the efficiency of carbon monoxide photoproduction in the St. Lawrence estuarine system (Canada). Environ. Sci. Technol. **40:** 7771–7777, doi:10.1021/es0615268